Effects of buoyancy and thermophysical property variations on the flow of supercritical carbon dioxide

Jundi He, Junjie Yan, Wei Wang, Peixue Jiang, Shuisheng He

Effects of buoyancy and thermophysical property variations on the flow of supercritical carbon dioxide

Jundi He[a], Junjie Yan[b], Wei Wang[c], Peixue Jiang[b], Shuisheng He[a,*]

[a]*Department of Mechanical Engineering, University of Sheffield, Sheffield, UK, S1 3JD*
[b]*Department of Energy and Power Engineering, Tsinghua University, Beijing, China, 100084*
[c]*Scientific Computing Department, Science and Technology Facilities Council, Warrington, UK, WA4 4AD*

Abstract

The flow and heat transfer behaviours of fluids at supercritical pressure have been studied using direct numerical simulations (DNS), in which one or more thermal properties are artificially frozen to discern the various physical mechanisms from each other so as to better understand the complex phenomena. Different from previous similar studies on this topic, this study focuses on the axial flow development resulted from the large variations of thermophysical properties. The contribution of the flow inertia has been quantified by analysing the momentum balance for each case studied, which has been found to be significant throughout the entire length of the pipe in cases when buoyancy is considered. The effect of the inertia on momentum in turn impacts on turbulence production, generally delaying flow laminarisation. Such an influence of flow development is non-trivial and cannot be omitted in flow analysis and heat transfer calculations. This suggests that the results of simplified analyses based on a spatially developed flow cannot be directly applied to such flows despite they can be very useful in developing fundamental understanding of the physics. Similarly, this also explains that in some cases, buoyancy parameters based on local flow quantities cannot describe heat transfer deterioration accurately. The effect of variable viscosity alone can cause turbulence reduction by flattening the velocity profile, but it will not turn the velocity profile to an M-shape, which can only be achieved

---

*Corresponding author
Email address: s.he@sheffield.ac.uk (Shuisheng He)

by buoyancy.

1. Introduction

There are wide applications of fluids above the critical pressure in the energy industry. Examples of such systems include Supercritical Water-cooled Reactor (SCWR)—a type of advanced nuclear reactor, and supercritical CO_2 power cycles for extracting geothermal energy or the solar energy, or for coupling with an advanced gas-cooled nuclear reactor. With increasing temperature, supercritical-pressure (SCP) fluids will not change phase, but the thermophysical properties may change significantly and non-linearly. This may strongly influence the heat transfer behaviour and turbulent characteristics in a flow system, the understanding of which is still incomplete.

In early experimental studies, flows of different SCP fluids have been investigated. Bourke et al. (1970) carried out a number of experiments on SCP CO_2 with different conditions and found that in a heated upward flow, heat transfer coefficient was reduced, and suggested that this was linked to the change of density and viscosity and the effect of buoyancy. By analysing the experimental data, Ackerman (1970) suggested that this abnormal heat transfer behaviour is similar to the well-known film boiling. Some further experiments (Shiralkar and Griffith, 1970; Yamagata et al., 1972; Jackson et al., 1989) were carried out to investigate different factors that influence the heat transfer behaviour in vertical pipe flows of SCP fluids. In these experiments, temperatures were measured by calibrated thermocouples. Various correlations were obtained to describe such heat transfer behaviours. Kurganov and Kaptil'Ny (1992) conducted several experiments of vertical pipe flows of SCP CO_2 at different Reynolds numbers, with local velocity measurements using Pitot tubes inserted in the flow, and local temperature measurements with thermocouples. The results were compared with numerical predictions from the Popov turbulence model (Popov et al., 1977) with the consideration of the variation of thermophysical properties. Compared to the experimental data, the numerical solutions could not reflect the heat transfer deterioration, which the authors attributed to the failure of the modelling of the turbulence Prandtl number. Jackson et al. (2003) reported experiments of vertical pipe

flows of CO_2 just above and below the critical pressure. It was found that heat transfer deterioration and recovery were strongly affected by buoyancy. Strong buoyancy effect occurred when the critical temperature was between the bulk and wall temperatures, but when both the bulk and wall temperatures were above the critical temperature, buoyancy effect was relatively minor.

Literature surveys on early experimental studies have been done by Pioro et al. (2004) and Duffey and Pioro (2005) to summarise the knowledge obtained from the experimental studies. Pioro et al. (2004) collected the heat transfer correlations from early studies and compared their predictions with experimental data. They have found that only some of the correlations show similar results to the experimental data. Duffey and Pioro (2005) went through 450 papers on the experiments of SCP CO_2. The majority of these experiments were for vertical pipes, and some were for horizontal pipes. The authors re-iterated the classification of the heat transfer modes of heated SCP fluid flows as normal, deteriorated, and improved heat transfer. Deteriorated heat transfer mode usually appears in higher wall heat flux and lower mass flux flows. Recent experimental studies by Yan et al. (2018) and Jiang et al. (2019) studied the heat transfer characteristic of n-decane at supercritical pressure. Yan et al. (2018) experiments mainly looked at the instability of supercritical fluid flows, and found that the transition to turbulence at the downstream is one of the reasons of the instability. The instability of the flow is weaker at higher pressures, higher mass flow rates, and higher inlet temperatures. Jiang et al. (2019) studied the heat transfer features of supercritical n-decane in rotating centrifugal channels, with varied rotating speed, mass flow rate, inlet temperature and heat flux. Jiang et al. (2019) found that heat transfer deterioration is weakened by the strong centrifugal force and flow deceleration.

For horizontal pipe flows, Tian et al. (2018) has done experiments of supercritical R134 flows with varying diameter, heat flux and mass flux. It was found that the buoyancy criteria based on supercritical water is not applicable to organic fluids, thus a new parameter was developed and validated against their own experimental data and those from previous literature. A set of experiments of supercritical R134 flows in horizontal pipes was obtained in Tian et al. (2019) to provide heat transfer data and correlations for further studies. A non-uniform circumferential wall temperature distribution was observed in these results, which can be attributed to the effect of buoyancy. For the bottom wall, the Dittus-Boelter type correlations are

3

acceptable, implying that the flow behaves as forced convection for the top surface of the horizontal pipe flows, the authors developed a new correlation based on a buoyancy parameter.

In spite of the difficulties, some attempts have been made to gain information on the flow and thermal fields through measurements. Vukoslavčević et al. (2005) designed and constructed a two-sensor hot-wire probe, and used it to measure the velocity and temperature of SCP CO_2 simultaneously for the first time. Optical measurements including Laser Doppler Velocimetry (LDV) and Particle Image Velocimentry (PIV) were also used to record and visualise the velocity field of SCP fluid flows (Ashkenazi and Steinberg, 1999; Licht et al., 2009; Valori et al., 2019), providing detailed flow data for studying the variations of turbulent characteristics. The difficulties of the acquisition of turbulent velocity and temperature fields due to the high pressure and high temperature environments and strong optical-index fluctuations with temperature prevent further studies into the details of the heat transfer deterioration and recovery of SCP fluid flows. Computational fluid dynamics (CFD) provides an alternative, efficient and powerful way for the studies of the abnormal heat transfer and turbulent behaviour in such fluid flows. In CFD studies, more flow details can be accessed with a lower cost compared to experiments. The numerical approach has become increasingly more popular with the advancement of high-performance computers, which provide high-speed computation capabilities. Bellmore and Reid (1983) used an early numerical model to predict the wall temperature of an upward pipe flow of para-hydrogen just below the critical pressure. Density fluctuations were taken into consideration in the governing equations for compressible flows, and the turbulence viscosity was modelled by the mixing length theory. The predicted wall and bulk temperatures agreed with the experimental data, and the "M" shaped velocity profiles were reflected in the simulations. Koshizuka et al. (1995) carried out CFD simulations of cooled vertical pipe flows of SCP water using a steady-state solver with the standard $k-\epsilon$ turbulence model . They also considered the variable thermophysical properties. The correlations of mass flux and heat flux obtained from the CFD simulations agreed well with those from the experiments (Yamagata et al., 1972). In these numerical studies, when the heat flux was significantly above the value of the deteriorated heat transfer mode, there were spacial oscillations in the resolved temperature profiles, and the simulations were highly unstable. Two explanations were proposed to explain the heat transfer deterioration of the heated SCP flow: (i) low near-wall viscosity leads to lower Prandtl numbers,

which leads to thicker thermal boundary layers and smaller Nusselt numbers, with the heat transfer deteriorated; (ii) the near-wall flow is accelerated due to the strong buoyancy, and then the streamwise velocity profile is flattened with a low wall-normal gradient and thus lower turbulence production. This understanding and explanation of the heat transfer deterioration provide an important reference for further investigations on vertical flows of SCP fluids. Lee and Howell (1998) conducted a similar numerical study using a modified mixing length turbulence model to simulate the convective heat transfer of fluids near the critical point. The numerical model could capture the general feature of SCP flows and showed good agreement with the experimental data. It was found that one of the effects of property variations is to delay the flow developing process and the flow reaches the fully-developed state in a longer distance.

He et al. (2005) used a number of low-Reynolds number eddy-viscosity turbulence models to simulate SCP CO_2 in a vertical pipe. The simulations reproduced most of the general features observed in previous experiments, and it was found that in a pipe with a small diameter, the buoyancy effect is not significant, but there is still heat transfer deterioration. This is because of the streamwise acceleration caused by the thermophysical property variations (significant reduction of density and viscosity). In addition, He et al. (2005) compared the ability of different 2-equation turbulence models to predict the SCP fluid flows. Most of the turbulence models assessed can reproduce the general trend of heat transfer deterioration caused by the buoyancy, but significant quantitative differences between the predictions of these models were observed. The comparison of Reynolds-averaged Navier-Stokes (RANS) simulations using a number of low-Reynolds number turbulence models with DNS to assess the ability of the former to predict the heat transfer and turbulence of SCP flow were carried out by He et al. (2008). It is found that the V2F model produces the most reliable predictions, and most turbulence models can reproduce the diminished turbulence kinetic energy to some extent, but not the recovery of heat transfer. To some extend, this could be attributed to the constant turbulence Prandtl numbers that were used to calculate the turbulence heat flux in these turbulence models. Pucciarelli et al. (2015) also tested the performance of several two-equation turbulence models, i.e., the AKN (Abe et al., 1995) model, the Deng et al. (2001) model, and the low-Reynolds $k - \epsilon$ model in solving the heat transfer of supercritical fluids, and found that the three models behave similarly, all of them are sensitive to the crossing of the critical temperature, and the recovery is

not well predicted, because the turbulence production due to buoyancy is not taken into account. Adding the Algebraic Heat Flux Model (AHFM) can help these turbulence models to better predict the recovery phase. The capabilities and limitations of such Algebraic Heat Flux Model were further tested and discussed by Pucciarelli et al. (2016), and compared with DNS data. The model prediction agreed reasonably well with DNS though, Pucciarelli et al. (2016) pointed out that further improvement can be obtained by selecting a case-specific AHFM parameter for different turbulence models. Xu et al. (2018)' recent study supports the above conclusions drawn by He et al. (2008) and Pucciarelli et al. (2015). Recognizing that the inaccurate prediction of turbulence production and the use of constant turbulent Prandtl number are major factors for the failure of RANS turbulence models in solving supercritical fluid flows, Jiang et al. (2018) developed a new modified model, with an improved model for buoyancy production and a variable turbulent Prandtl number. The new model was adopted in the AKN $k - \epsilon$ model (Abe et al., 1995), and and showed improved performance in terms of solving supercritical fluid flows with strong heating.

In addition to RANS simulations, direct numerical simulations (DNS) of heated vertical pipe flows of SCP CO_2 were carried out by Bae et al. (2005). A more detailed picture of SCP flows can be captured by DNS. The well-known heat transfer deterioration in upward pipe flows and the recovery of heat transfer rate were shown to be directly linked to the reduction and recovery of turbulence, and the buoyancy production were important under some conditions. DNS investigations to vertical annular flows with a heated inner wall were carried out by Bae et al. (2008). It was shown that near the hot wall, the normalised streamwise velocity profiles are not logarithmic any more because the turbulent shear stress near the wall is largely reduced. Another observation was that the high-speed and low-speed fluctuating velocity streaks disappear at the locations of the heat transfer deterioration, and turbulence activities such as sweep and ejection are largely weakened at this stage of the flow. The DNS of pipe flows of strongly heated air was also conducted by Bae et al. (2006) to study the effect of thermophysical property variations. Similar turbulence and heat transfer reduction were observed, and the mean velocity and temperature profiles were found to be dissimilar with each other at down-stream locations. It is of interest to note that the low Mach number approximation was applied in the governing equations used in Bae et al. (2005), following Accary et al. (2005). This method is different from the incompressible approach where the compressibility is

completely ignored. With the low Mach number approximation, the simulations can predict the analytical convection threshold in Rayleigh–Bénard configuration. Some other DNS studies of supercritical fluid flows are done by Li et al. (2007) and Chu and Laurien (2016). Li et al. (2007) simulated channel flows of supercritical carbon dioxide, with a heated and a cooled wall. The flow is similar to that in a annular flow simulated by Bae et al. (2008). The distance between the high- and low-speed streaks in the cooling region increases and turbulence is enhanced. It was found that the compressibility effect linked to the pressure fluctuation and dilatation of velocity fluctuation could be ignored, while the buoyancy production was significant, due to strong density fluctuations. Chu and Laurien (2016) simulated a horizontal pipe flow of supercritical carbon dioxide, which confirmed the observations made by Tian et al. (2019). The wall temperature was again found to be higher at the top due to the secondary flow caused by buoyancy. Interestingly, without the buoyancy effect in the streamwise direction, a reduction in turbulence and heat transfer coefficient still happen due to the variations of thermophysical properties. Nemati et al. (2016) carried a DNS on the effect of imposing different thermal wall boundary conditions, i.e., with and without enthalpy fluctuations at the pipe wall. It was shown that the heat transfer in SCP fluids can be significantly influenced by the thermal boundary conditions. With/without enthalpy fluctuations at the wall, and hence the density and viscosity fluctuations can influence the turbulent shear stress and turbulent heat flux.

From the conclusions of previous experimental and numerical studies, the effects that cause the abnormal heat transfer and turbulence behaviour in SCP fluids in vertical pipes are mainly: (i) buoyancy (non-uniform body force) effect, (ii) acceleration due to density reduction and (iii) effect of other variable thermophysical properties. In the present study, these three effects are investigated using direct numerical simulations (DNS) with artificially varied conditions to eliminate or isolate some effects. Similar research methodology has been seen in a numerical study of heated and cooled annular channel flow of SCP CO_2 (Peeters et al., 2016). In that work, simulations with constant thermophysical properties, or with only variable density, or with only variable viscosity, or with variable thermophysical properties with and without gravity, were carried out to study the effects. The simulations were carried out under the condition of fully developed flows, and hence any entrance effects are excluded. Mean velocity and turbulent shear stress profiles were significantly affected by the variations of density and viscosity.

7

The change of velocity gradient increases the production of turbulent kinetic energy near the cold wall, but decreases it near the hot wall.

Another DNS study that is relevant to the present study is (He et al., 2016), who studied non-uniform body force (i.e., the buoyancy) effect using an artificially prescribed body force distributions simulating buoyancy. This enables them to study the buoyancy force under an isothermal condition. A new interpretation was proposed for flow laminarisation caused by non-uniform body forces such as buoyancy. It was found that the turbulent shear stress of a body force influenced flow can be expressed as a summation of that of a flow of the same pressure gradient (EPG) but without any body forces, and an additional shear stress attributed to the body force. We will further discuss this idea together with the analysis of our results later in this paper.

The current study aims at investigating the effects of various physical mechanisms/processes on heat transfer and turbulence in an upward pipe flow of SCP CO_2. The techniques used in Peeters et al. (2016) to eliminate or isolate different effects will be used here. In Jurriaan's work (Peeters et al., 2016) on an annular flow, the inner and outer walls were set to hot and cold respectively and the net heat input to the flow was zero. Consequently, there was no flow development in the axial direction, which significantly simplified the flow phenomena. In this study, we apply a constant heat flux on the pipe wall and the flow development along the pipe is a major characteristic of the flow as in many experiments. We expect significant differences between developing and fully-developed SCP fluid flows, which is one of the focuses of this study.

2. Methodology

Direct numerical simulations (DNS) are carried out in the present study using an in-house code CHAPSim (Seddighi, 2011; He and Seddighi, 2013; Wang and He, 2015). It is based on a low Mach number approximation and considering the enthalpy dependence variable thermophysical properties (NIST database, Lemmon et al. (2010)). The governing equations are as follows:

Continuity equation:

$$\frac{\partial \rho}{\partial t} + \frac{\partial (\rho u_j)}{\partial x_j} = 0 \tag{1}$$
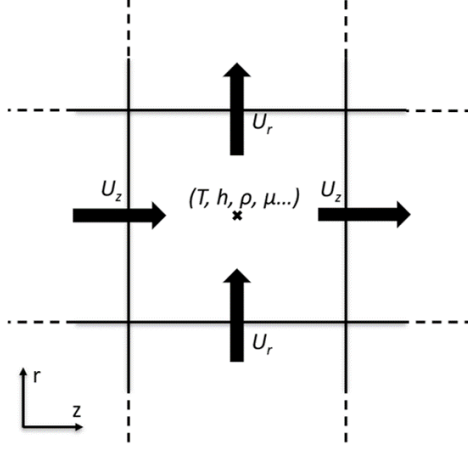
Figure 1: Thermal and motion variable definitions in the finite-difference mesh

Momentum equation:

$$\frac{\partial(\rho u_i)}{\partial t} + \frac{\partial(\rho u_i u_j)}{\partial x_j} = -\frac{\partial p}{\partial x_i} + \frac{1}{Re_0}\frac{\partial \tau_{ij}}{\partial x_j} + \frac{\rho}{Fr_0^2} \quad (2)$$

Energy equation:

$$\frac{\partial(\rho h)}{\partial t} + \frac{\partial(\rho h u_i)}{\partial x_i} = \frac{1}{Re_0 \cdot Pr_0}\frac{\partial}{\partial x_i}\left(\lambda\frac{\partial T}{\partial x_i}\right) \quad (3)$$

The finite difference scheme is used for the spatial discretisation of the governing equations and a low storage 3rd order explicit Runge-Kutta (RK3) scheme for the time discretisation. The momentum equations and energy equations are solved with half a time step staggered with each other. In the simulation mesh, the scalar variables are defined at the cell centre, and velocity components are defined at the cell faces. The locations of thermal and flow variables in z and r (streamwise and radial) directions are shown in figure 1.

The velocities and other variables are normalised as follows:

$$u_i = \frac{u_i^*}{u_{z,0}^*}, x_i = \frac{x_i^*}{R^*}, t = \frac{t^* u_{z,0}^*}{R^*}, p = \frac{p^*}{\rho_0^* u_{z,0}^{*2}} \quad (4)$$

where subscript "0" denotes the inlet value, superscript "∗" denotes the dimensional values. The thermophysical properties are normalized by the

inlet values, except the enthalpy, which is normalized in a different way (h^*_{ref} is the enthalpy at $650K$ and $8.57MPa$):

$$\rho = \frac{\rho^*}{\rho^*_0}, \lambda = \frac{\lambda^*}{\lambda^*_0}, \mu = \frac{\mu^*}{\mu^*_0}, c_p = \frac{c^*_p}{c^*_{p0}}, T = \frac{T^*}{T^*_0}, h = \frac{h^* - h^*_{ref}}{c^*_{p0}T^*_0} \qquad (5)$$

As a result of the above normalisation, the non-dimensional parameters appearing in the governing equations (the inlet Reynolds number Re_0, the inlet Prandtl number Pr_0 and the inlet Froude number Fr_0) are based on inlet thermal properties:

$$Re_0 = \frac{\rho^*_0 u^*_{z,0} R^*}{\mu^*_0}, Pr_0 = \frac{\mu^*_0 c^*_{p0}}{\lambda^*_0}, Fr_0 = \sqrt{\frac{u^{*2}_{z,0}}{g^* R^*}} \qquad (6)$$

To produce instantaneous fully-developed turbulent velocity profiles for the inlet of the heating section, a periodic, isothermal turbulence generator is running parallelly with the heating section.

To determine the local properties, the pressure is assumed to be constant, so that the thermophysical properties are functions of only the enthalpy. The properties are obtained using the NIST database (Lemmon et al., 2010).

The statistical values in the present study are extracted after the flow has reached a stationary state in time and all the statistical values are averaged in time and circumferentially, as the time averaged flow is expected to be axi-symmetric.

To validate the capability of CHAPSim in solving the turbulent pipe flow, the isothermal turbulent pipe flow carried out by El Khoury et al. (2013) ($Re_\tau = 180$) was reproduced by CHAPSim. The results including the time averaged streamwise velocity $\overline{u^+_z}$, and the root mean square of fluctuating velocities u^+_{rms} in three directions agree very well with those from the above reference (figure 2).

The validation of CHAPSim in terms of solving SCP fluid flows is shown next. Two cases with strong heating and buoyancy from the simulations of Bae et al. (2005) (case B and D) have been chosen to be reproduced by CHAPSim. These two cases have also been reproduced by Nemati et al. (2015), using another DNS code, to compare the capabilities of different DNS codes. For the simulations of case B and D carried out by Bae et al. (2005), the mesh size is $769 \times 69 \times 129$ in streamwise, radial and spanwise direction, the reproduction done by Nemati et al. (2015) has a mesh size of $768 \times 68 \times 128$, while the cases reproduced by CHAPSim have the mesh size
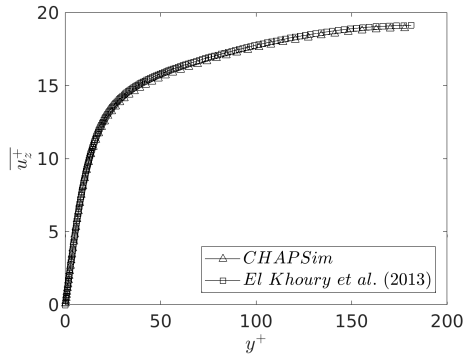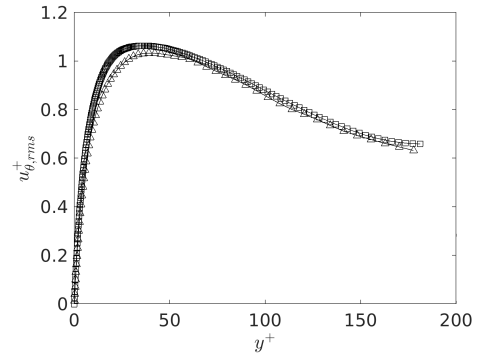
(a) Streamwise velocity
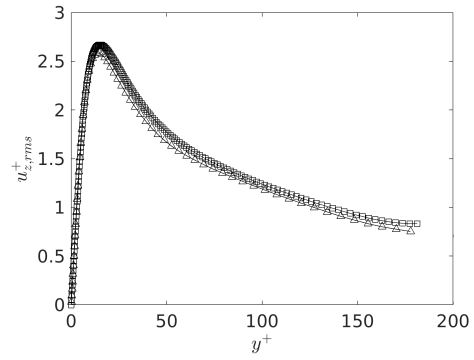
(b) Streamwise fluctuating velocity
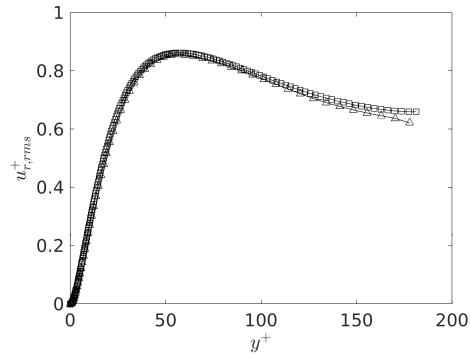
(c) Radial fluctuating velocity

(d) Spanwise fluctuating velocity

Figure 2: Comparisons of streamwise velocities, root mean square of fluctuating velocities at streamwise, radial, and spanwise directions of a isothermal pipe flow ($Re_\tau = 180$), results obtained by code CHAPSim and El Khoury et al. (2013)
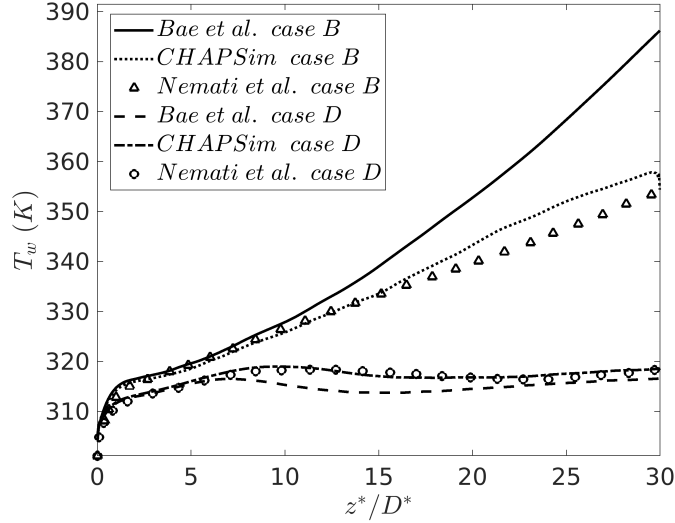
Figure 3: Comparison of wall temperature predictions obtained by CHAPSim against results obtained by Bae et al. (2005) and Nemati et al. (2015)

of $768 \times 64 \times 128$. The resolved streamwise profiles of wall temperatures of these two cases, obtained by CHAPSim, Bae et al. (2005), and Nemati et al. (2015), are shown in figure 3. The results from simulations using all three DNS codes for case D seem to agree very well with each other, where for case B, CHAPSim's result and that of Nemati agree well but Bae predicted a higher wall temperature. The difference may be due to the use of different thermal property tables and numerical methods. In any case, the overall agreement is considered to be satisfactory.

3. Case settings

From previous studies, it is known that the factors that influence the heat transfer behaviours and turbulence characteristics are mainly the buoyancy and the variations of thermophysical properties. The latter can be split into: the acceleration caused by density reduction and the variations of viscosity and thermal conductivity. In this study, we are particularly interested in the response of the momentum equation and its influences on turbulence reduction and regeneration. For this purpose, we have designed a number of numerical simulation cases, listed in table 1 to isolate or eliminate some of the effects of interest for investigation.

Table 1: Simulation case setting

Case	Flow condition	Convection type
A	Supercritical CO_2 (base case)	Mixed convection
B	Supercritical CO_2 (forced convection)	Forced convection
C	Supercritical CO_2 (only density varies)	Mixed convection
D	Supercritical CO_2 (only density constant)	Forced convection
E	Supercritical CO_2 (Boussinesq approximation)	Mixed convection
F	Supercritical CO_2 (isothermal)	Forced convection

Case A is a reference case for an upward pipe flow of supercritical carbon dioxide, with strong and non-linear variations of thermophysical properties under strong heating. Case B is the same as case A, except that the gravity (and hence the buoyancy) is removed, that is, the flow is forced convection. In case C, all the thermophysical properties except density, are constant. Consequently, in this case, only the effects linked to density variations are included (buoyancy and acceleration effects). In case D density is made constant but all other thermophysical properties are enthalpy dependent as in case A. Case E is based on the Boussinesq assumption, that is, all properties are constant except the density in the gravity which is dependent on the enthalpy. Case F is another reference case with all the thermophysical properties set constant.

The mesh size for all cases is $1024 \times 64 \times 128$ in streamwise, radial and spanwise direction. The same inlet and boundary conditions are imposed for all the cases. The inlet pseudocritical pressure is $8.57 MPa$, and the inlet temperature is $301.15K$, and for comparison, the critical temperature at this pressure is 310.9 K. The inlet Reynolds number is 2617 (or 5234 based on the diameter), and the inlet Prandtl number is 2.86. A uniform heat flux of $30870W/m^2$ is applied on the wall. The density and dynamic viscosity variations against the temperature, for CO_2 at $8.57MPa$, are shown in figure 4a, and the thermal conductivity and specific heat against temperature are shown in figure 4b. The figures shows that for a supercritical fluid, a small change in temperature can cause huge changes in thermalphysical properties around the pseudo-critical state, which is the key reason for the abnormal turbulence and heat transfer features.
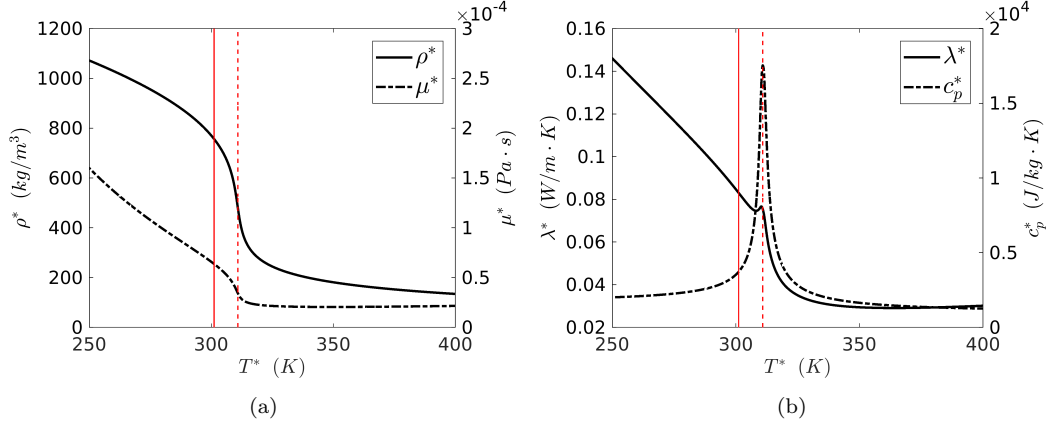
Figure 4: Variations of density, dynamic viscosity (a), thermal conductivity and specific heat against temperature (b) for CO_2 at $8.57MPa$ (data from NIST database). The solid and the dashed line show the inlet and pseudo-critical temperatures, respectively.

4. Result and discussions

4.1. An overview of flow and heat transfer behaviour in a supercritical CO_2 flow (case A)

In this discussion, two types of average schemes are used: the Reynolds average with an over-bar denoting the averaged value, and a superscript $'$ denoting the fluctuating component; and the Favre average (density-weighted average), with a tilde denoting the averaged value, and a superscript $''$ denoting the fluctuating component:

$$\phi = \overline{\phi} + \phi' \quad \phi = \widetilde{\phi} + \phi'' \tag{7}$$

In this section, the flow and heat transfer feature of case A will be presented and discussed. This is the only case in which a physical pipe flow of SCP CO_2 under heating is simulated. In all other cases, there are always some selected effects that are eliminated or isolated artificially. Early experimental and numerical studies indicate that in an upward pipe flow of SCP fluids, heat transfer deterioration often takes place, which is then followed by recovery. Such heat transfer behaviour can be largely related to flow laminarisation followed by turbulence regeneration. The result of case A simulation exhibits such behaviours. Figure 5a shows the streamwise development of wall and bulk temperatures. The pseudo-critical temperature is about $310.9K$. After a short distance from the inlet, the wall temperature
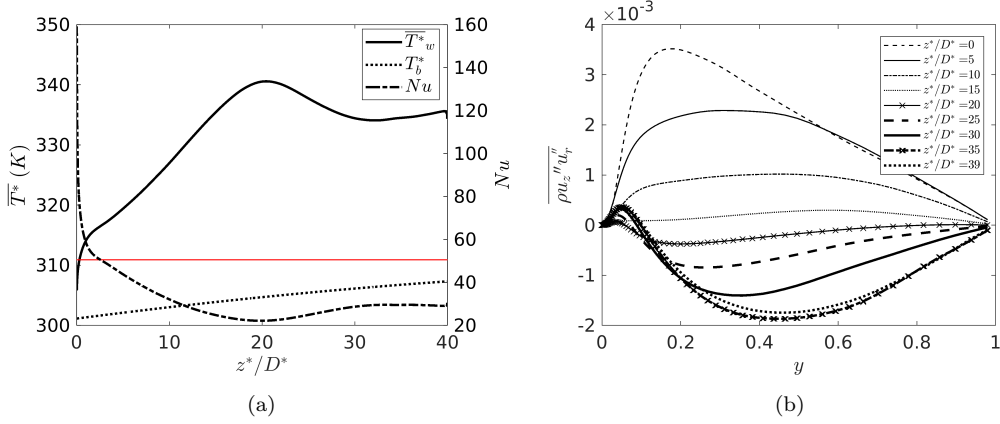
14

Figure 5: Streamwise distributions of wall temperature, bulk temperature, and Nusselt number in case A (a), pseudo-critical temperature is marked by a red solid line. Radial profiles of Favre averaged normalised turbulent shear stress $\overline{\rho u_z'' u_r''}$ at several streamwise locations in case A (b).

is above the critical value, while the bulk temperature is still below that. Right after the inlet, the Nusselt number reduces rapidly in a short distance, while the wall temperature increases rapidly. This is due to the entrance effect, where a thermal boundary layer is formed, which grows rapidly in this region. After the entrance region, the Nu continues reducing, and T_w increases, all at a rate slower than before. T_w reaches the peak at about the same streamwise location as Nu reaches the minimum value, at around $z^*/D^* = 20$. After this location, Nu starts to increase and heat transfer improves, thus the wall temperature reduces even as the bulk temperature is still growing linearly. These trends agree with those observed from early experimental and numerical studies. The radial profiles of Favre averaged turbulent shear stress at several streamwise locations are plotted in figure 5b. Before $z^*/D^* = 15$, the turbulent shear stress reduces with distance from the entrance. At around $z^*/D^* = 15$, turbulent shear stress is nearly zero at most part, which suggests that the flow is fully laminarised at this location. This is strongly linked to the heat transfer deterioration. After $z^*/D^* = 15$, the magnitude of turbulent shear stress rises again, but in most part, the turbulent shear stress is negative, different from that of the isothermal pipe flow. Under this condition, turbulence is mostly produced in a region away from the wall where the velocity gradient has changed sign due to the M-shape as shown below.

(a) Streamwise velocity

(b) Temperature
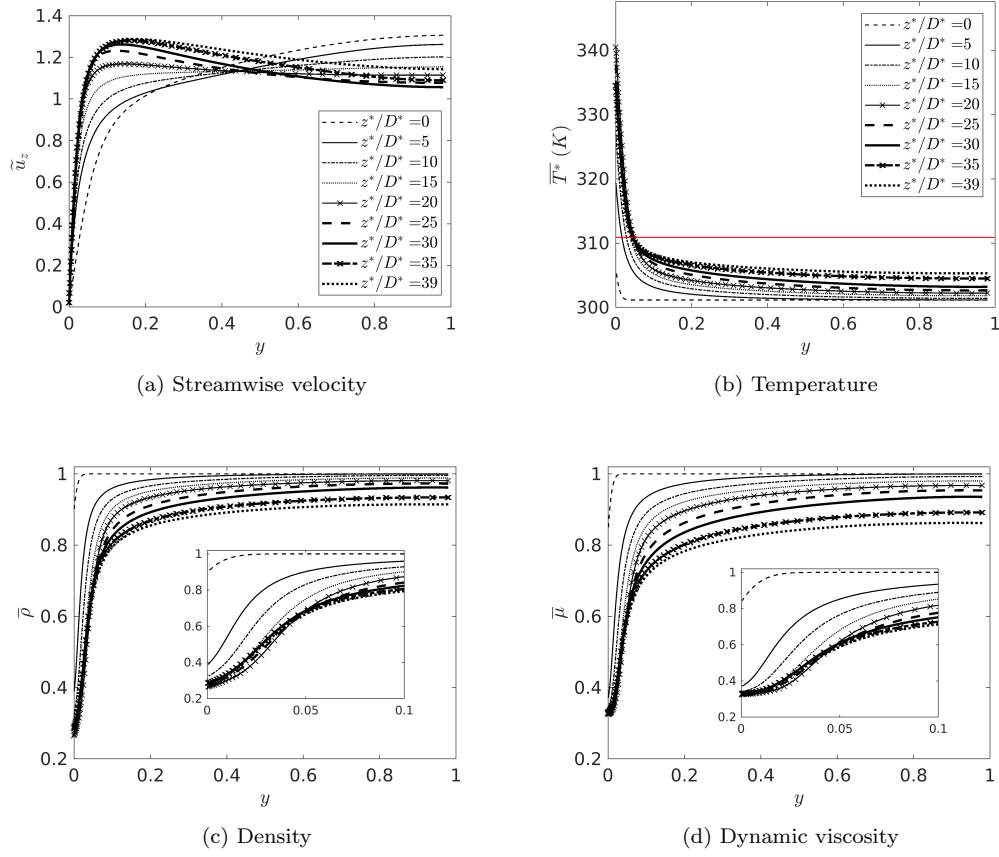
(c) Density

(d) Dynamic viscosity

Figure 6: Radial profiles of streamwise velocity (a), temperature (b), density (c), and dynamic viscosity (d) in case A

The radial profiles of streamwise velocity, temperature, density, and dynamic viscosity at several streamwise locations are shown in figure 6. The development of the streamwise velocity is key to the variations of turbulence and heat transfer. At the inlet, the velocity profile is one of a typical fully-developed turbulent profile. Due to a number of reasons to be discussed later, the near-wall fluid accelerates, and that in the core decelerates relatively. As a result, the velocity profiles become increasingly flattened in the core of the flow. This continues until $z^*/D^* = 15$, where the wall-normal velocity gradient is nearly zero everywhere in the flow, except for very close to the wall. The near-wall acceleration and main stream deceleration continue, further downstream, and the velocity profile flips from a flat profile into an "M" shaped one. Here a negative velocity gradient is shown in the central region of the "M" shape profile. Such a flow behaviour is caused by the combination of a number of reasons, including the buoyancy effect, the acceleration due to the density reduction (both local and bulk acceleration), and the rapid and non-uniform (in radial direction) reduction of dynamic viscosity, which will be discussed in the next section.

Also shown in figure 6 are the temperature profiles which show that a thermal boundary layer is rapidly developed after the inlet, causing strong variations of temperature near the wall. In the core of the flow, the temperature gradually increases axially, but the radial gradient does not change much. The wall temperature is above the critical temperature, but in the core ($y > 0.1$), the temperature is lower than the pseudo-critical value, which indicates there are significant variations of thermophysical properties between the near-wall and mainstream locations. The profiles of averaged density (figure 6c) and dynamic viscosity (figure 6d) clearly support this observation. The variations of density and dynamic viscosity profiles are very similar to each other with strong changes in the near-wall region. The lowest density near the wall has dropped to nearly 30% of that at the inlet and the dynamic viscosity has dropped to nearly 35% of that at the inlet. For the properties at the center of the pipe, the reduction is less severe. The density at the outlet is about 90% of the inlet density, and the viscosity is about 85% of the inlet value. The large radial gradient of density causes a strong radially non-uniform buoyancy. The large radial gradient of the dynamic viscosity is another factor, which influences the shear stress especially at the near-wall region.

With such significant changes of thermophysical properties in case A, the flow and heat transfer behaviour is drastically different from that of

the isothermal flow, or even that of a heated flow below the pseudocritical pressure.

4.2. Comparison of cases with different effects

The overall influences of different thermo-properties and buoyancy on the flow and turbulence are discussed in this section by studying the simulation cases, in which various combinations of property changes are omitted to isolate certain physical phenomenon. The streamwise velocity profiles of cases B to E are shown in figure 7, which can be compared with that in Case A in figure 6a. It can be clearly seen that the behaviours of the mean velocity show two strikingly different responses. First, the velocity profiles in Cases B and D are similar to each other but different from those in other cases. In Case D (constant density), the profile becomes flatter in the core of the flow within a short distance ($\Delta z^*/D^* < 5$) after the flow is heated and then remains largely unchanged afterwards. This initial change is due to the reduction of viscosity close to the wall as a result of the increase in fluid temperature there. This will be further discussed in the next section. In Case B (forced convection), the velocity profile also becomes flatter in a short distance from the start of the heating. Following this, it increases continuously with distance downstream, though the shape appears to be largely maintained. This increase in bulk velocity is clearly due to the decrease in density as the bulk fluid temperature increases.

On the other hand, the developments of the velocity profiles in Cases C and E are very similar in a qualitative way, to that in Case A, in which the profile first becomes increasingly more flattened. Then at a later stage, it gradually switches to an M-shaped profile, which becomes increasingly more prominent downstream. Noting that these three flows are the only cases with buoyancy, this result implies that buoyancy causes the strongest distortion in velocity distribution and is a necessary condition for the switch of the profile to a M-shape (at least under the conditions studied). Additionally, the switch of the shape of the profile occurs first in Case A ($z^*/D^* \sim 15$), then Case C ($z^*/D^* \sim 20$) and then Case D ($z^*/D^* \sim 30$), which suggests that other effects (viscosity variation and flow acceleration due to the expansion of the fluid) all contribute to the distortion of the velocity profile.

The streamwise developments of the turbulent shear stress for cases B, C, D, and E are shown in figure 8. Considering the similarities of streamwise velocity, it is now not surprising to note that the developments in cases B and D are similar to each other but different from those of cases C and E.

In Case B, $\overline{\rho u_z'' u_r''}$ reduces gradually over the distance of $z^*/D^* < 15$, after which it appears to have reached some equilibrium and remains largely unchanged afterwards. It is somewhat surprising that $\overline{\rho u_z'' u_r''}$ in Case D also reduces significantly in the initial section ($z^*/D^* < 15$) which is only slightly smaller than that in Case B, even though the velocity profile in this case does not change following the initial adjustment ($z^*/D^* < 5D$). The above result appears to suggest that the variation of viscosity has a stronger effect on turbulence than that of flow acceleration. In cases C and E, $\overline{\rho u_z'' u_r''}$ undergoes the full process of progressively reduction initially, followed by a near all zero distribution over the whole cross-section (full laminarisation) and finally recovery, as in Case A. The location where the flow is fully laminarised approximately corresponds to the location where the velocity profile switches to the M-shape. In addition, the negative value of the $\overline{\rho u_z'' u_r''}$ at the final stage is highest in Case A, then C and then D, again implies that the viscosity and flow acceleration all have an influence on the flow and turbulence, even though the buoyancy is clearly dominating. These results imply that the simulation using Boussineq approximate is able to capture the key phenomenon, including turbulence reduction and heat transfer deterioration, but quantitatively the predictions may suffer from significant uncertainties, predicting a late heat transfer deterioration, for example, which may be undesirable in some applications.

The profiles of the root mean square of the three fluctuating velocity components are shown in figures 9 to 11. Again the variations of these quantities in Cases B and D are similar to each other, and those in Cases A, C and E are similar. The effects of the buoyancy, variation of viscosity and flow acceleration (due to density change) can be observed in a similar way as that in the $\overline{\rho u_z'' u_r''}$ while comparing the results in the various cases, which are not repeated here. However, there are some additional interesting observations which are worthwhile noting. Firstly, the peak value of u_z' in Cases B and D reduces to its lowest values soon after $z^*/D^* = 5$, whereas at these locations, u_r' and u_θ' largely remain unchanged or even with a slight increase in some cases. It takes up to $z^*/D^* = 20$ before these quantities reach their final values. This is a reflection of the turbulence structure changes. Secondly, the u_z' in Case D remains largely unchanged shortly after $z^*/D^* = 5$ whereas the peak of u_z' in Case B gradually recovers downstream to a value close to its inlet one. This is likely to be linked to the flow acceleration near the wall, but it does not have resonance in u_r' and u_θ'. Finally, all these turbulence quantities reduce initially, reaching a significant lower value at between $z^*/D^* = 15$ and
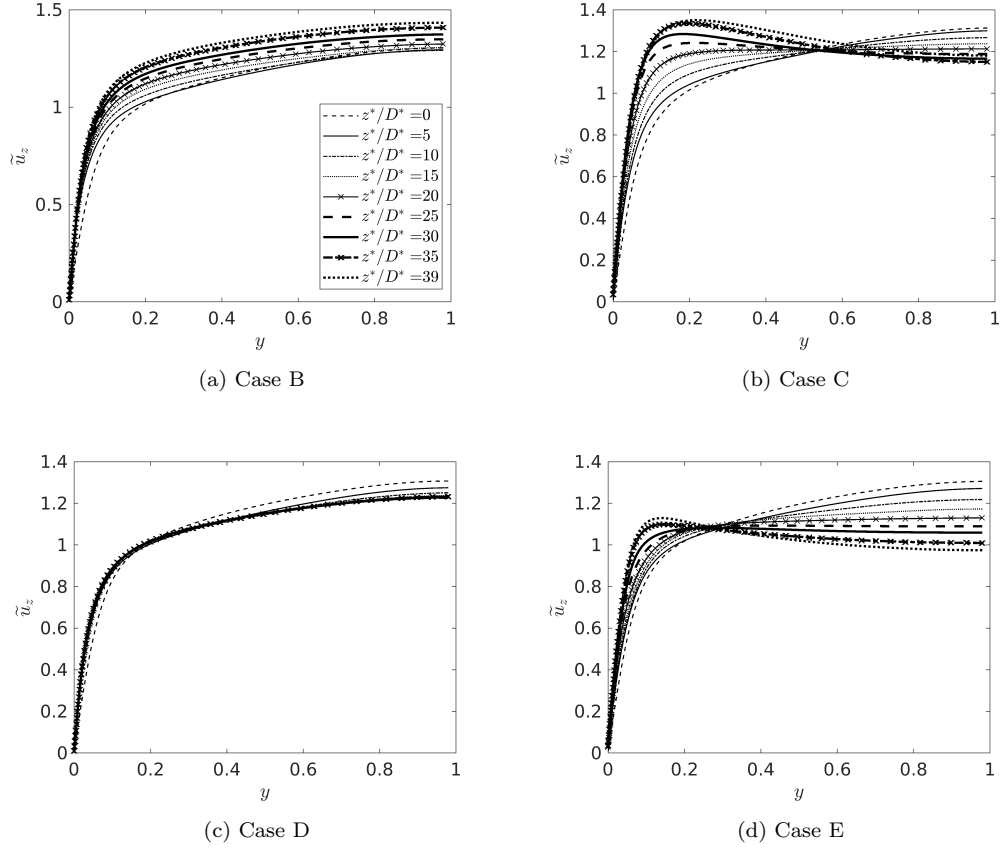
(a) Case B

(b) Case C

(c) Case D

(d) Case E

Figure 7: Radial profiles of Favre averaged streamwise velocities of case B (a), case C (b), case D (c), and case E (d).

(a) Case B

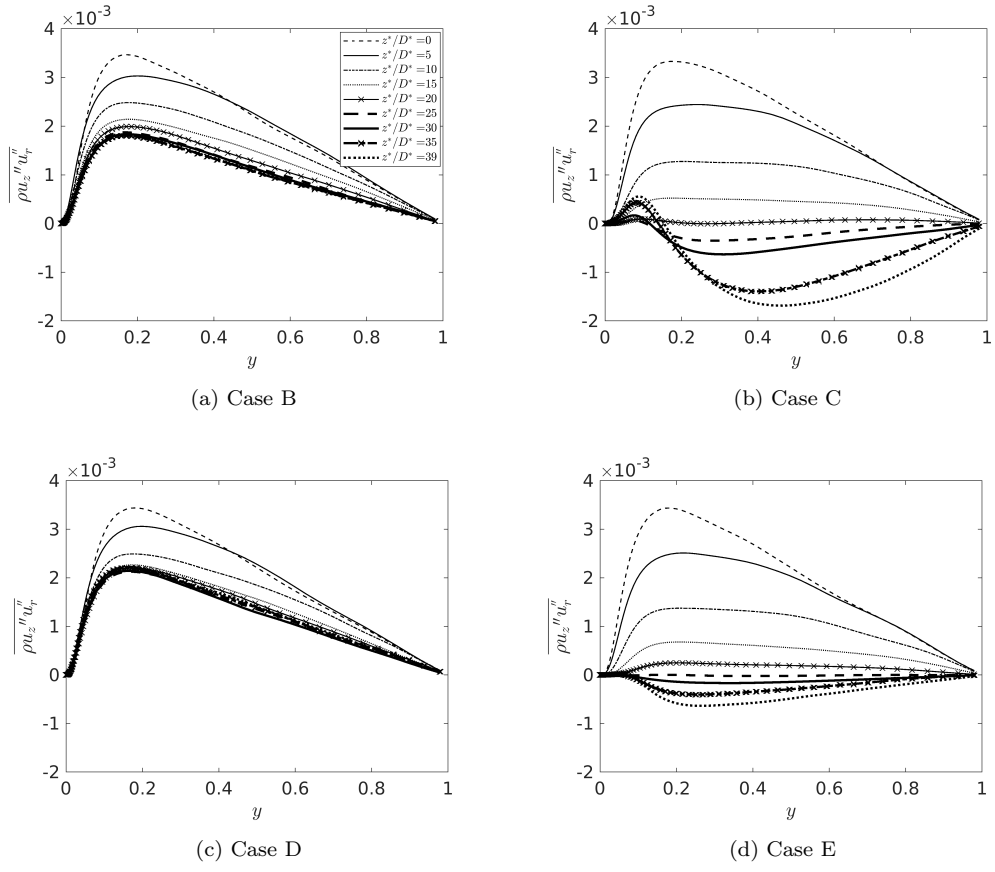(b) Case C

(c) Case D

(d) Case E

Figure 8: Radial profiles of Favre averaged turbulent shear stress of case B (a), case C (b), case D (c), and case E (d).

21

30 depending on the cases, and then start to recover. It is however important to note that even at the location where $\overline{\rho u''_z u''_r}$ is near zero, the magnitudes of all the three fluctuating velocities are still very significant. In fact, the peak of u'_z reduces by about half, whereas the reduction of the peaks of the u'_r and u'_θ is much stronger, to about a third at the lowest point.

Finally, we study the influences of the above changes in turbulent characteristics on heat transfer. The streamwise profiles of the wall temperatures and Nusselt numbers in Cases A to E are plotted in figure 12. In all cases, the wall temperature increases rapidly within about $z^*/D^* = 2$ reflecting the rapid establishment of the thermal boundary layer at the start of the heating, and correspondingly the Nusselt number reduces rapidly from a very high initial value. Note that the top of the Nusselt number plot is clipped off for the benefit of more clearly showing the variations at later stages. From the wall temperature and Nusselt number profiles, it is clear that cases A, C, and E all experience heat transfer deterioration and recovery, and that case A has the strongest and earliest reduction, followed by case C, then case E. This again suggests that both the variation of thermal property and flow acceleration have some influence on heat transfer although the strongest effect comes from buoyancy. The result of case D indicates that the variation of thermal properties with constant density causes a small reduction in Nusselt number. It is surprising that even though the turbulence is generally speaking much stronger in case B than in Case E, but the variation of the Nusselt number is very similar in the two cases. The variation of thermal conductivity can contribute towards the observation. In case B, when the temperature reaches the pseudocritical value, there is a significant local reduction in thermal conductivity near the wall, which worsens the heat transfer, while in case E, the thermal conductivity is constant everywhere.

4.3. Turbulence modification due to the viscosity variation (Case D)

From the above discussion, it is clear that the buoyancy has the largest effect in the flows with strong thermophysical property variations studied herein, though the changes in other thermal properties can also cause partial laminarisation. The mechanisms of the laminarisation caused by the viscosity variation and buoyancy effects will be investigated in section 4.3 and 4.4. The question we ask is that for a given thermal field (and hence variations of properties and buoyancy), how will the flow and turbulence respond? To answer this question, we study the balances of the terms in the streamwise momentum equation in Cases D, and A & E to understand the evolution of
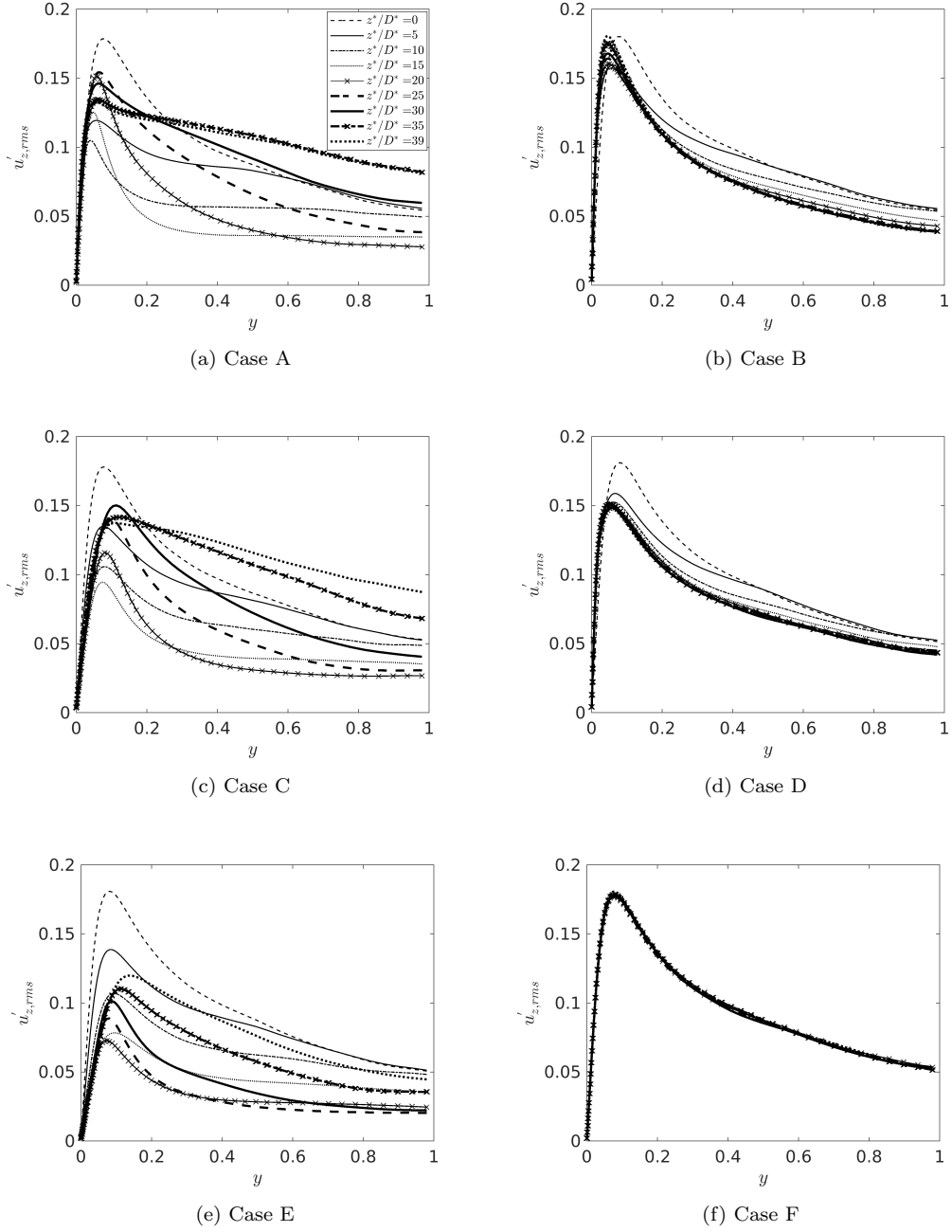
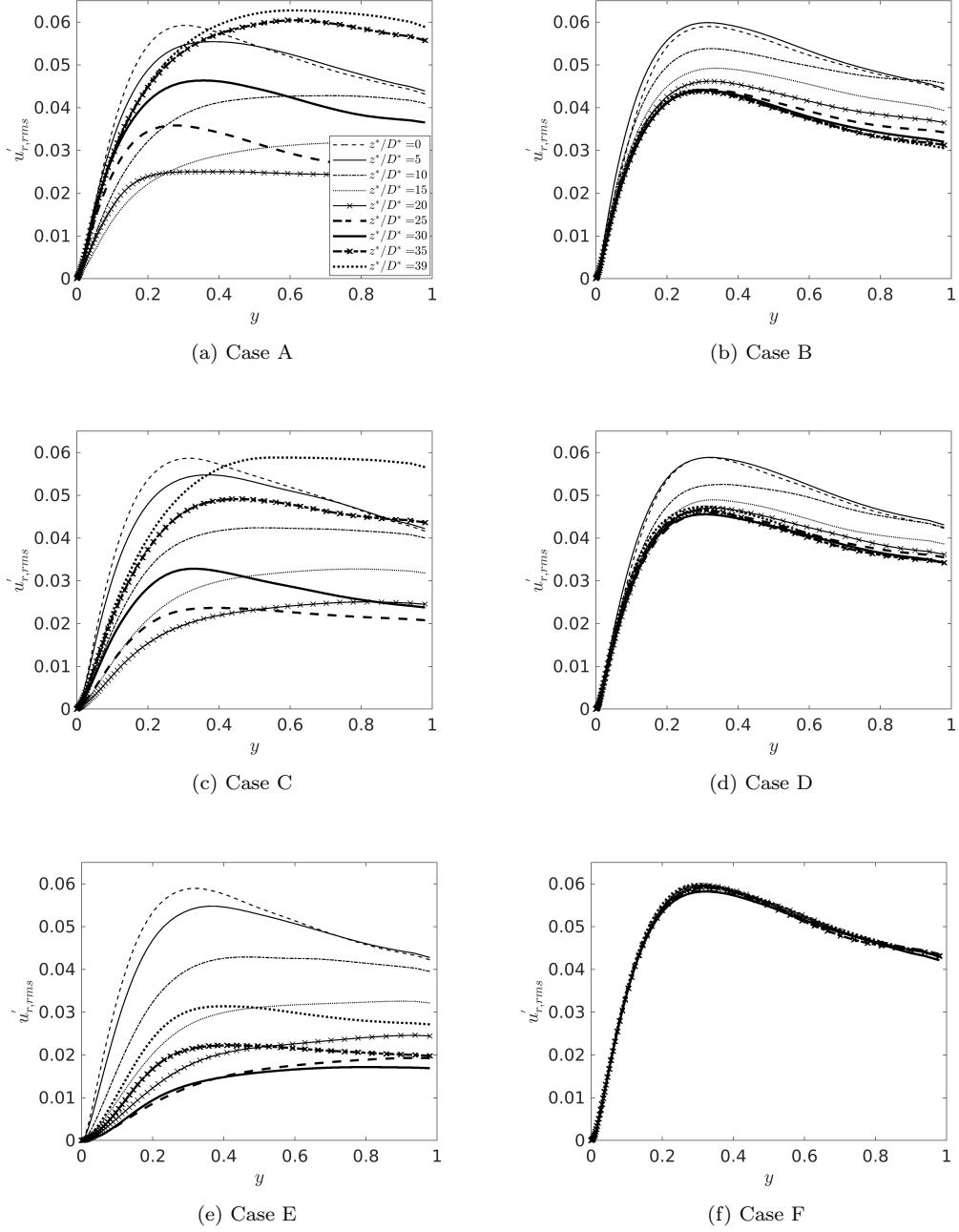Figure 9: Radial profiles of the r.m.s of the streamwise fluctuating velocity in all cases.

(a) Case A

(b) Case B

(c) Case C

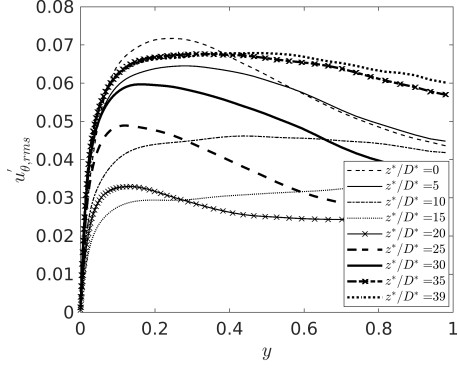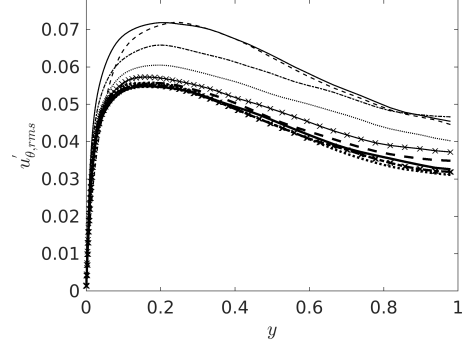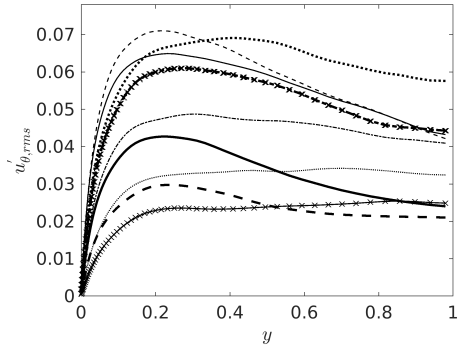(d) Case D

(e) Case E

(f) Case F

Figure 10: Radial profiles of the r.m.s of the radial fluctuating velocity in all cases.
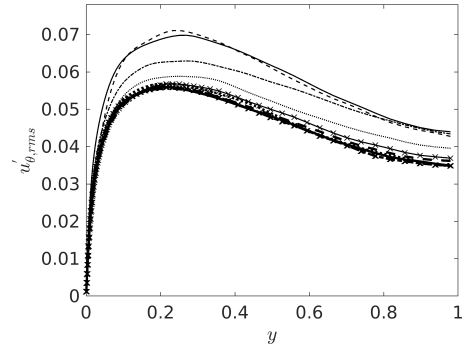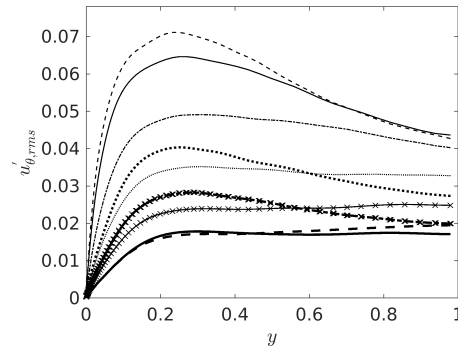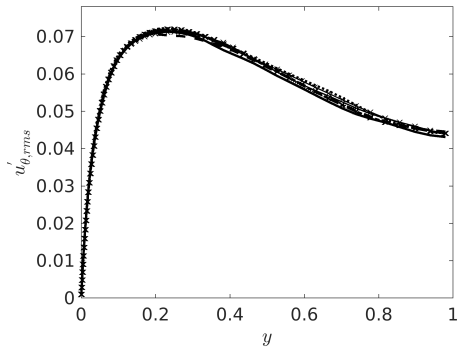
(a) Case A

(b) Case B

(c) Case C

(d) Case D

(e) Case E

(f) Case F

Figure 11: Radial profiles of the r.m.s of the spanwise fluctuating velocity in all cases.
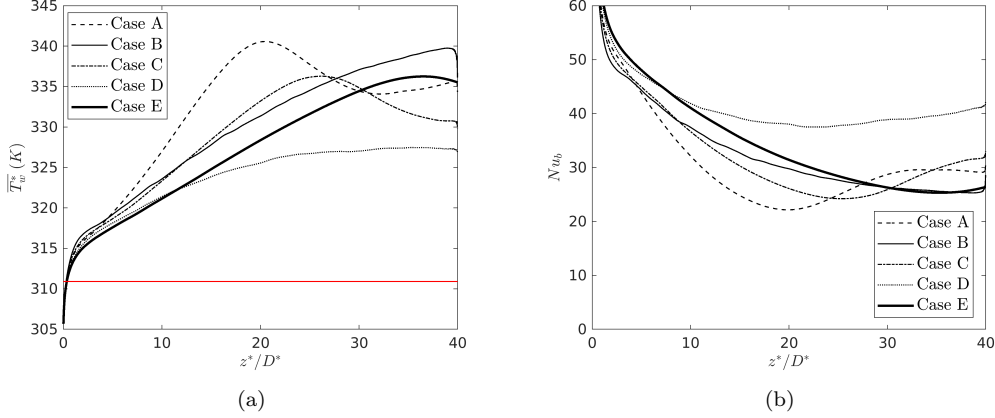
Figure 12: Streamwise distributions of wall temperature (a), pseudo-critical temperature is specified by a red solid line, and Nusselt numbers (b) for case A to E.

the various terms along the flow. Case D is only affected by the viscosity variation, which causes the flow to be partially laminarised; whereas in cases A (base case) and E (Boussinesq), turbulence is affected by strong buoyancy effect (and other effects in Case A), and the flow undergoes full laminarisation followed by recovery with regeneration of turbulence.

We first focus on Case D to study the effect of viscosity. The axial developments of the radial profiles of the temperature and viscosity are shown in figure 13. The wall temperature rises above the critical value $(310.9K)$ at an early stage $(z^*/D^* < 2)$, and the thermal boundary layer is quickly established. After this initial rapid development, the thermal boundary layer appears to largely maintain its shape while the temperature increases very much at the same rate across the radius of the pipe. This implies that the thermal field has achieved some kind of fully-developed state. Due to the strong variation of viscosity with temperature especially around the pseudo-critical point, the viscosity experiences drastic variations close to the wall, in a way that mimics the thermal boundary layer. The viscosity at the wall reduces to about 35% of that at the inlet. It is useful to note that even though the viscosity in the core of the flow reduces progressively downstream, the value close to the wall appears to maintain largely unchanged after $z^*/D^* = 5$. This is because the viscosity of the fluid passing the pseudocritical point (i.e., the gas-like fluid) does not change significantly with temperature any more as shown in figure 4a.
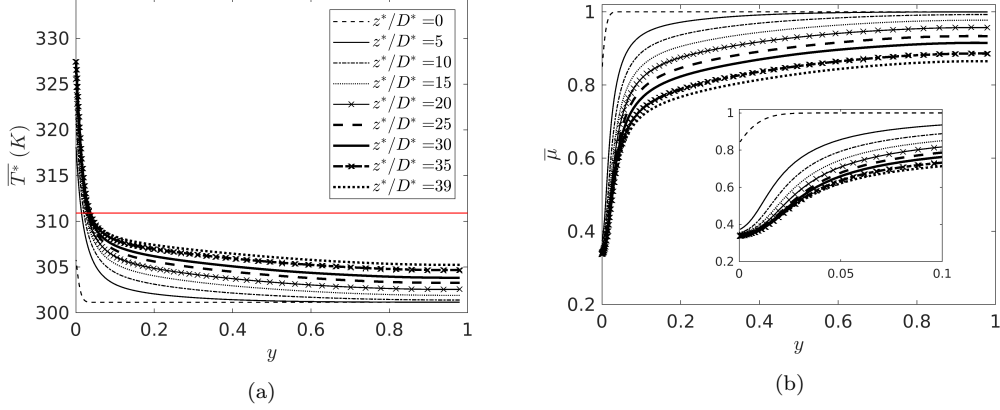
26

Figure 13: Radial profiles of temperature (pseudo-critical temperature is specified by a red solid line) and normalised dynamic viscosity at several streamwise locations of case D

We consider the flow to have reached a stationary state and note that the flow is axi-symmetric, and hence the following momentum equation:

$$
\begin{aligned}
\frac{\partial(\rho u_z)}{\partial t} = &- \frac{\partial(\rho u_z u_z)}{\partial z} - \frac{1}{r}\frac{\partial(r\rho u_r u_z)}{\partial r} - \frac{1}{r}\frac{\partial(\rho u_\theta u_z)}{\partial \theta} \\
&- \frac{\partial p}{\partial z} - \rho g \\
&+ \frac{1}{Re_0}\left(\frac{\partial}{\partial z}\left(2\mu\frac{\partial u_z}{\partial z}\right) + \frac{1}{r}\frac{\partial}{\partial r}\left(r\mu\left(\frac{\partial u_r}{\partial z} + \frac{\partial u_z}{\partial r}\right)\right) + \frac{1}{r}\frac{\partial}{\partial \theta}\left(\mu\left(\frac{\partial u_\theta}{\partial z} + \frac{1}{r}\frac{\partial u_z}{\partial \theta}\right)\right) \right)
\end{aligned}
\tag{8}
$$

can be averaged azimuthally and over time. To find the momentum balance over the fluid from the pipe centre to a radius r, we multiply r over both sides of the equation, then integrate every term from the pipe centreline ($r = 0$) to the location (r), then dividing the resultant equation by r. For case D (constant density) and case E (Boussinesq assumption), it follows that the

27

above streamwise momentum equation becomes:

$$
\begin{aligned}
0 = &\underbrace{-\frac{1}{r}\int_0^r r\frac{\partial(\rho_0 \overline{u}_z\,\overline{u}_z)}{\partial z}dr}_{IN1}\ \underbrace{-\ \rho_0\overline{u}_z\,\overline{u}_r}_{IN2}\\[4pt]
&\underbrace{-\frac{1}{r}\int_0^r r\frac{\partial(\rho_0\overline{u_z' u_z'})}{\partial z}dr}_{TS1}\ \underbrace{-\ \rho_0\overline{u_z' u_r'}}_{TS2}\\[4pt]
&\underbrace{+\frac{1}{Re_0}\Big(\frac{1}{r}\int_0^r r\frac{\partial}{\partial z}\big(2\overline{\mu}\frac{\partial\overline{u}_z}{\partial r}\big)dr}_{VS1}\ \underbrace{+\ \overline{\mu}\big(\frac{\partial\overline{u}_r}{\partial z}+\frac{\partial\overline{u}_z}{\partial r}\big)\Big)}_{VS2}\\[4pt]
&\underbrace{-\frac{r}{2}\frac{\partial P}{\partial z}}_{PG}\ \underbrace{-\frac{1}{r}\int_0^r r(\overline{\rho}-\overline{\rho}_c)gdr}_{Bo}
\end{aligned}
\tag{9}
$$

where ρ_0 and ρ_c represent the density at the inlet and the pipe centreline, respectively, and $\frac{\partial P}{\partial z}\equiv(\frac{\partial\overline{p}}{\partial z}+\frac{\overline{\rho}_c}{Fr_0^2})$ is the modified pressure gradient. From left to right, the equation includes, two inertial terms ($IN1$ and $IN2$), two turbulent shear stress terms ($TS1$ and $TS2$), the viscous shear stresses ($VS1$ and $VS2$), and finally the (modified) pressure gradient term (PG) and the buoyancy term (Bo). The terms $TS1$ and $VS1$ have been found to be always negligibly small and are therefore omitted in the following figures and discussion for clarity.

Now let $r = R$ to consider the momentum balance for the entire cross section, in which case the turbulence terms and $IN2$ will disappear. However, unlike a fully developed flow, $IN1$ may not necessarily be zero as will be seen later. Hence:

$$
0 = \underbrace{-\frac{1}{R}\int_0^R r\frac{\partial(\rho_0\overline{u}_z\,\overline{u}_z)}{\partial z}dr}_{IN1}\ \underbrace{-\frac{\partial P}{\partial z}\frac{R}{2}}_{PG}\ \underbrace{-\frac{1}{Re_0}\overline{\mu}\big(-\frac{\partial\overline{u}_z}{\partial r}\big)_{r=R}}_{VS2}\ \underbrace{-\frac{1}{R}\int_0^R r(\overline{\rho}-\overline{\rho}_c)gdr}_{Bo}
\tag{10}
$$

The momentum balance (Eq 9) for Case D at a number of axial locations are shown in Figure 14, in which $y = 0$ is represented by eq. 10. The balance for the non-heating section is also shown (in red) for comparison. For such isothermal flows, the only non-zero terms are the viscous ($VS2$) and the turbulent shear stress ($TS2$), and the pressure gradient (PG) and the gravity (Bo). In Case D in which the density is unchanged, Bo is zero.

28

Let us consider a location soon after the start of the heating (e.g. at $z^*/D^* = 5$). The viscosity of the fluid at the wall reduces sharply as shown in figure 14, which causes a reduction in frictional resistance on the wall. This directly causes the driving force, pressure gradient, to reduce, which in turn causes the fluid in the core of the flow to decelerate since nothing else (i.e., the viscous or turbulent stresses) has changed at this early stage. In fact, the deceleration directly balances the reduction in pressure gradient. In the region adjacent to the wall however, the reduction in viscous force due to the reduced viscosity prevails the reduction in pressure force and the fluid accelerates. This explains the large values and the distribution of the inertia term $IN1$. The dis-synchronized acceleration/deceleration in the core and wall regions naturally necessitates a net radial flow to maintain continuity, resulting in the second non-zero inertial term ($IN2$). It is useful to note at this point that the large reduction in viscosity on the wall is not completely accommodated by the reduction in pressure gradient. As a result of the non-uniform flow acceleration/deceleration across the radius, the velocity gradient on the wall is significantly increased which compensates the reduction in viscosity to some extent. Hence the actual change in both the wall shear and the pressure gradient at this location ($z^*/D^* = 5$) is less than 30%. It is also interesting to note that the inertial term IN1 is non-zero at the wall due to the redistribution of the velocity profile despite the bulk velocity remains unchanged streamwise.

A consequence of the velocity redistribution is that the velocity profile becomes flatter than in an isothermal flow (see fig 7c). This can also be understood knowing that the viscosity is much lower closer to the wall and a large velocity gradient is required to compensate for the reduction in viscosity for the same shear stress. It is well known that a flattened velocity profile will cause a reduction in turbulence production (Bae et al. (2005)), which explains the partial flow relaminarisation caused by variable viscosity such as that in Case D. This contrasts the scenario when the viscosity is reduced across the entire pipe, which will lead to an increase in Reynolds number and turbulence.

Next, we recall the fact that much of the reduction in viscosity near the wall occurs within $z^*/D^* < 5$, with only small changes later. The velocity, however, takes much longer to adjust due to inertia which is significant over a distance up to around $z^*/D^* = 10$. The response of turbulence appears occurs between $z^*/D^* = 5$ and $z^*/D^* = 15$. This, therefore, suggests that the entrance development is largely governed by the flow characteristics rather
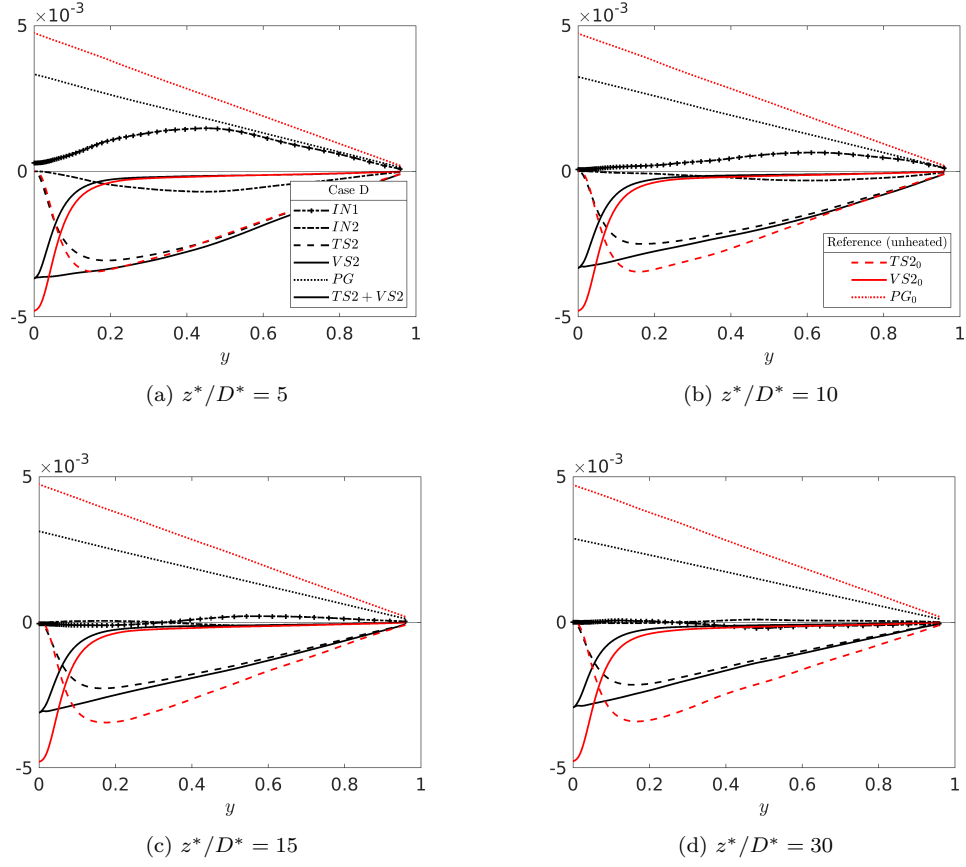
29

Figure 14: Radial profiles of the streamwise momentum equation balance at z^*/D^*=5 (a), 10 (b), 15 (c), 30 (d), in case D (black lines), in comparison with the budget profiles before the heating section (red lines).

than the thermal field, despite the initial cause is the change in viscosity due to temperature variations. The absence of the changes in viscosity downstream explains the significant observation that the flow can reach a fully developed state over most part of the pipe (e.g. $z^*/D^* > 15$). This is expected to be a common phenomenon for flows where the wall temperature is above the pseudocritical value. For the flows where the wall temperature is below the T^*_{pc}, the viscosity may vary significantly as the flow and thermal fields develop, which may, in turn, lead to a continuing developing flow.

4.4. Laminarization due to buoyancy and other effects combined (Cases A, C and E)

We begin with Case E, the momentum balance of which is shown in figure 15. Under Boussinesq assumption, all properties are constant except for the density in the gravitational term which varies with temperature. Hence the only effect considered in this case is buoyancy. In figure 15, both the modified pressure gradient (PG) and the total body force ($PG + Bo$) are shown to facilitate discussion.

First, again, consider a location at the start of the heating ($z^*/D^* = 5$ as an example). Strong buoyancy effects are present near the wall due to the rapid development of the thermal boundary layer, which accelerates the flow close to the wall. This directly results in a reduction in the pressure gradient under the condition of constant mass flux. Like in Case D, this reduced pressure gradient causes a deceleration in the core region (e.g., $y > 0.5$) since both the viscous and turbulence stresses are still unchanged at this stage. Different from the effect of variable viscosity though, buoyancy-induced flow acceleration near the wall results in an increase in the velocity gradient adjacent to the wall leading to an increase in the wall shear stress.

Further downstream, the buoyancy progressively increases and the modified pressure gradient reduces. In fact, it becomes negative somewhere between $z^*/D^* = 15$ and 20. The flow becomes effectively a buoyancy-driven flow and the velocity profile switches to M-shape for $z^*/D^* > 20$.

It is useful to note the important role the inertial terms play in this flow. The buoyancy together with the associated change in pressure gradient along the pipe tends to distort the velocity, but this is achieved through flow acceleration/deceleration. Figure 15 shows that such effect ($IN1$ and $IN2$) makes a big contribution to the momentum balance at the early stage of the heating section. Unlike in Case D, the effect continues playing a significant role throughout the pipe length. This suggests that any analysis based on

'equilibrium' concept, assuming the flow is fully developed in the flow direction (e.g., Peeters et al. (2016) & He et al. (2016)) cannot be directly applied to the spatially developing flow in practice, even though the fundamental understanding can well be used to assist in the analysis. This also explains that the use of the dimensional parameters such as Bo^* based on the local bulk properties may not represent the flow behaviour accurately.

We can, therefore, conclude that in an upwards heated pipe with buoyancy influence-only, the buoyancy effect comes into play through several routes: (i) the non-uniform body force distribution accelerates the flow near the wall; (ii) the pressure gradient reduces as a result of the increasing buoyancy force and hence leading to a relative deceleration in the core of the flow; and (iii) the inertia 'delays'/'lessens' the above effects. The combined effect is that the velocity profile is significantly flattened in the early stage of the heated pipe, which leads to a reduced turbulence production (Bae et al. (2005)).

It can be deduced by comparing figures 15 and 7d that the critical point where the velocity profile turns from an ordinary centre-peaked velocity to an M-shape occurs at the location when the modified pressure gradient approaches roughly zero. Following this point, the pressure gradient is opposing the flow whereas the net forward flow is driven by the buoyancy near the wall. Consequently the peak of the velocity occurs at a location away from the pipe centre. We can further deduce that the effect of variable viscosity however strong it might be will never turn the flow to M-shape since unlike the flow aiding buoyant force, it will only cause a reduction in the frictional resistance in the near-wall region.

Finally, we study the momentum balance in cases A and C, in which the density varies significantly. Consequently, the corresponding Favre averaged

formulation is used for the momentum equation:

$$
0 = \underbrace{-\frac{1}{r}\int_0^r r\frac{\partial(\overline{\rho}\widetilde{u}_z\,\widetilde{u}_z)}{\partial z}dr}_{IN1} \underbrace{-\overline{\rho}\widetilde{u}_z\,\widetilde{u}_r}_{IN2}
$$
$$
\underbrace{-\frac{1}{r}\int_0^r r\frac{\partial(\overline{\rho u_z'' u_z''})}{\partial z}dr}_{TS1} \underbrace{-\overline{\rho u_z'' u_r''}}_{TS2}
$$
$$
\underbrace{+\frac{1}{Re_0}\Big(\frac{1}{r}\int_0^r r\frac{\partial}{\partial z}\Big(2\overline{\mu}\frac{\partial\overline{u}_z}{\partial r}\Big)dr}_{VS1} \underbrace{+\overline{\mu}\Big(\frac{\partial\overline{u}_r}{\partial z}+\frac{\partial\overline{u}_z}{\partial r}\Big)\Big)}_{VS2}
$$
$$
\underbrace{-\frac{r}{2}\frac{\partial P}{\partial z}}_{PG} \underbrace{-\frac{1}{r}\int_0^r r(\overline{\rho}-\overline{\rho}_c)g dr}_{Bo}
$$

(11)

The general trend of the development of the momentum balance in Case C (figure 16) is similar to that observed in Case E, except for that the distributions of the inertial terms. In this case, the dominant inertial term ($IN1$) becomes negative close to the wall which continues up to the wall. In the final station, the term becomes negative throughout the pipe. This implies that the net effect of the velocity profile redistribution is that the momentum increases along with the flow even though the mass flux remains constant. The negative momentum inertia is clearly caused by flow acceleration due to the fluid expansion alongside the increase of the fluid temperature along with the flow.

The development of the momentum balance in Case A again follows a trend very similar to that observed in Case E (figure 17), though the changes are clearly stronger and occur earlier. We note the following key points: (i) The reduction of the modified pressure gradient reduces significantly faster under the combined action of all the three effects. Like in the cases discussed earlier, this is the cause for the velocity profile to distort, becoming more flattened in the core. The reduction in pressure also causes even stronger inertial terms, indicating that the flow is significantly different from the 'equilibrium' state, and the flow undergoes strong development axially. (ii) It is interesting to note that the wall shear stress in this flow does not deviate much from that of the isothermal flow. Clearly the effect of the viscosity (reducing the wall shear) and that of buoyancy (increasing the wall shear) have cancelled each

33

other to some extent as far as the wall shear stress, even though their effect on distortion of the velocity profile are in the same direction and reinforce each other. (iii) Similar to that in case C, the dominant inertial term ($IN1$) is negative in Case A even though at the earlier z stations, the region where it is negative is small. It, however, becomes more negative than in case C at later stations. Consequently, again the local acceleration/deceleration of the fluid in the process of distorting the velocity profile has a net effect of flow acceleration in a significant part of the flow.

5. Conclusions

Direct numerical simulations (DNS) have been carried out to study the flow and heat transfer behaviours of fluids at supercritical pressure. A number of simulations have been carried out with one or more thermal properties artificially frozen to isolate or eliminate some physical mechanisms to develop a better understanding of the complex phenomena. Different from previous similar studies on this topic (Peeters et al., 2016; He et al., 2016), we are particularly interested in the axial developing behaviours resulted from the large variations of thermal properties. The following conclusions can be drawn from the study:

- The flow inertia is significant in the momentum balance throughout the entire length of the pipe in any cases when the buoyancy is considered. This is largely due to the local (radially non-uniform) flow acceleration/deceleration due to the continuously varying buoyancy and viscosity (though the former dominates), leading to a continuously varying velocity profile along the flow. The contribution of the inertia has been quantified by analysing the momentum balance for each case studied.

- The effect of the inertia on momentum in turn impacts on turbulence production, generally delaying flow laminarisation. Such an influence of flow development is non-trivial and cannot be omitted in flow analysis and heat transfer calculations. This suggests that the results of simplified analyses based on a spatial developed flow (such as Peeters et al. (2016) and He et al. (2016)) cannot be directly applied to such flows despite they can be very useful in developing fundamental understanding of the physics. Similarly, this also explains that in some cases, buoyancy parameters based on location flow quantities cannot describe heat transfer deterioration accurately.
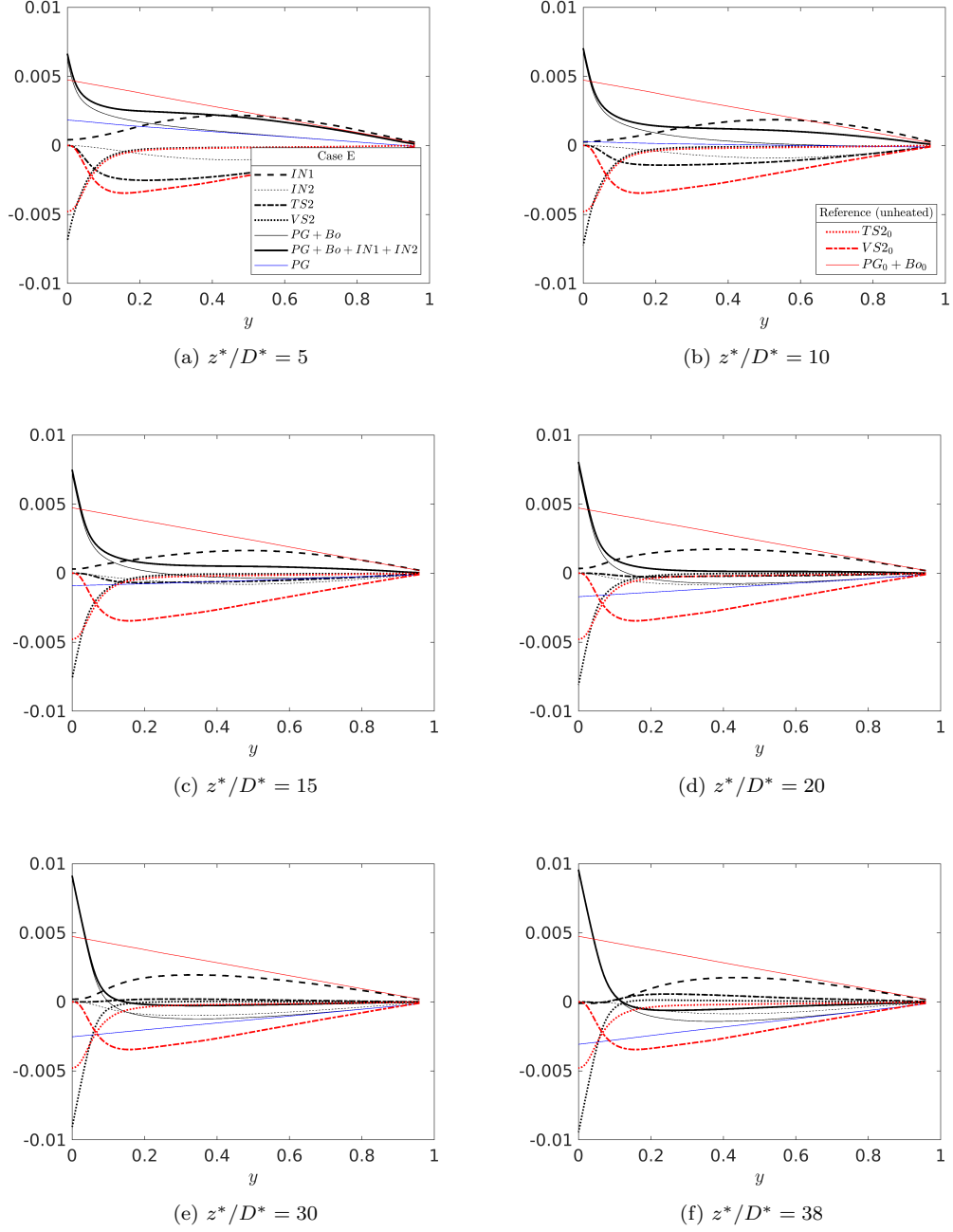
Figure 15: Balance of the streamwise momentum equation at several streamwise locations in comparison with the profiles before the heating (red), in case E (black).
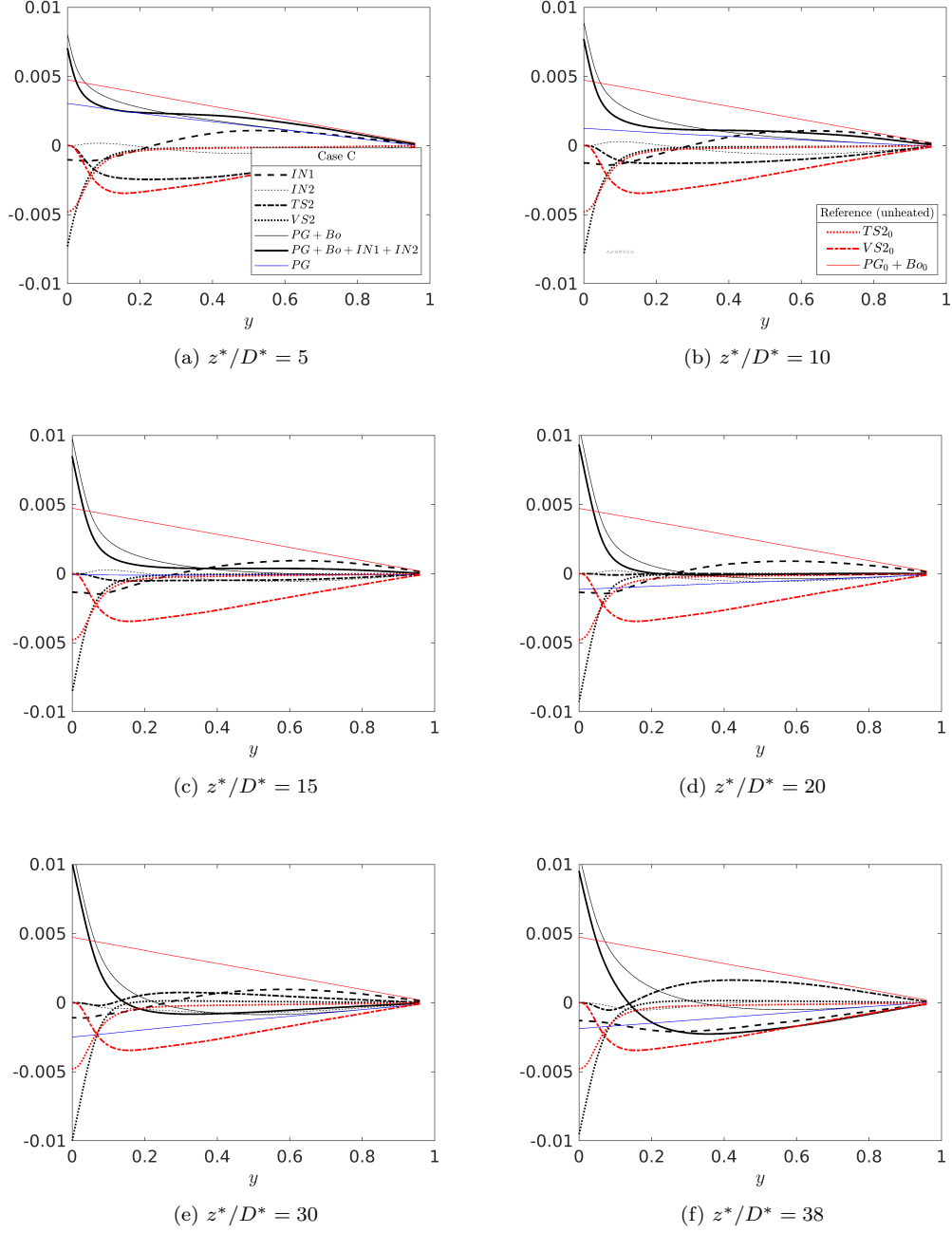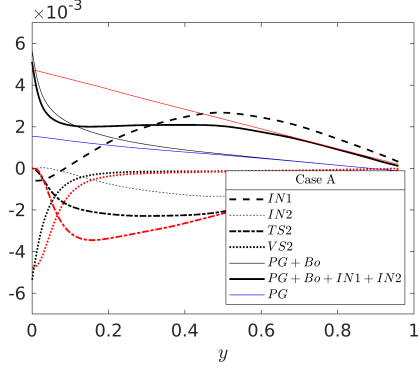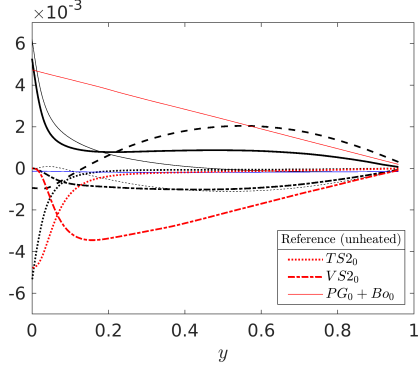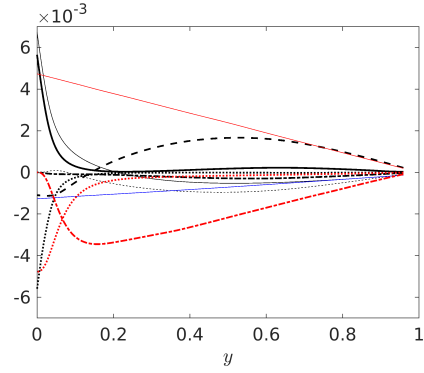
(a) $z^*/D^* = 5$

(b) $z^*/D^* = 10$

(c) $z^*/D^* = 15$

(d) $z^*/D^* = 20$

(e) $z^*/D^* = 30$

(f) $z^*/D^* = 38$

Figure 16: Balance of the streamwise momentum equation at several streamwise locations in comparison with the profiles before the heating (red), in case C (black).
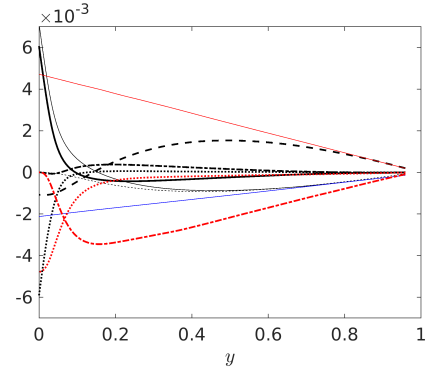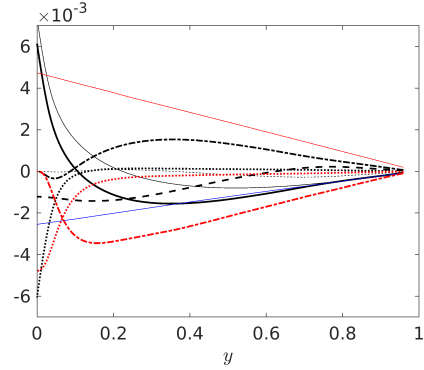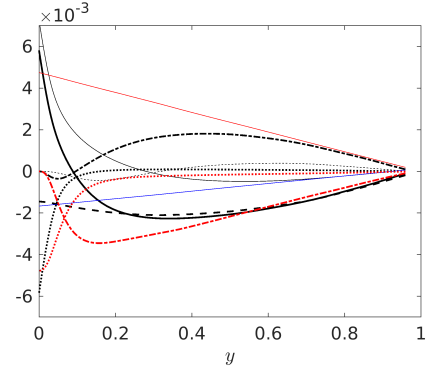
(a) $z^*/D^* = 5$

(b) $z^*/D^* = 10$

(c) $z^*/D^* = 15$

(d) $z^*/D^* = 20$

(e) $z^*/D^* = 30$

(f) $z^*/D^* = 38$

Figure 17: Balance of the streamwise momentum equation at several streamwise locations in comparison with the profiles before the heating (red), in case A (black).

- The effect of variable viscosity alone can cause turbulence reduction by flattening the velocity profile, but it will not turn the velocity profile to an M-shape, which can only be achieved by buoyancy. If the wall temperature is above the pseudo-critical temperature, the flow can achieve a fully developed state in which the flow and heat transfer behaviour remain largely unchanged expect in the entrance region.

- It has been shown that the use of Boussineq approximate is able to capture the key phenomenon in a heated upward flow of supercritical fluid, including turbulence reduction and heat transfer deterioration. However, there are large quantitative difference between the results of simulations using or not using this approximation, which suggests that the effect of viscosity and the general density variation (i.e., those in addition to the buoyancy) are also very strong and the use of Boussinesq approximation for the conditions such as those studied herein will cause some uncertainties in the predictions.

6. Acknowledgements

References

Abe, K., Kondoh, T., Nagano, Y., 1995. A new turbulence model for predicting fluid flow and heat transfer in separating and reattaching flows—ii. thermal field calculations. International Journal of Heat and Mass Transfer 38, 1467–1481.

Accary, G., Raspo, I., Bontoux, P., Zappoli, B., 2005. An adaptation of the low Mach number approximation for supercritical fluid buoyant flows. Comptes Rendus Mécanique 333, 397–404.

Ackerman, J., 1970. Pseudoboiling heat transfer to supercritical pressure water in smooth and ribbed tubes. Journal of Heat Transfer 92, 490–497.

Ashkenazi, S., Steinberg, V., 1999. High Rayleigh number turbulent convection in a gas near the gas-liquid critical point. Physical review letters 83, 3641.

Bae, J.H., Yoo, J.Y., Choi, H., 2005. Direct numerical simulation of turbulent supercritical flows with heat transfer. Physics of fluids 17, 105104.

Bae, J.H., Yoo, J.Y., Choi, H., McEligot, D.M., 2006. Effects of large density variation on strongly heated internal air flows. Physics of Fluids 18, 075102.

Bae, J.H., Yoo, J.Y., McEligot, D.M., 2008. Direct numerical simulation of heated co 2 flows at supercritical pressure in a vertical annulus at re= 8900. Physics of Fluids 20, 055108.

Bellmore, C., Reid, R., 1983. Numerical prediction of wall temperatures for near-critical para-hydrogen in turbulent upflow inside vertical tubes. Journal of Hear Transfer 105, 536–541.

Bourke, P., Pulling, D., Gill, L., Denton, W., 1970. Forced convective heat transfer to turbulent CO2 in the supercritical region. International Journal of Heat and Mass Transfer 13, 1339–1348.

Chu, X., Laurien, E., 2016. Flow stratification of supercritical CO2 in a heated horizontal pipe. The Journal of Supercritical Fluids 116, 172–189.

Deng, B., Wu, W., Xi, S., 2001. A near-wall two-equation heat transfer model for wall turbulent flows. International journal of heat and mass transfer 44, 691–698.

Duffey, R.B., Pioro, I.L., 2005. Experimental heat transfer of supercritical carbon dioxide flowing inside channels (survey). Nuclear Engineering and Design 235, 913–924.

El Khoury, G.K., Schlatter, P., Noorani, A., Fischer, P.F., Brethouwer, G., Johansson, A.V., 2013. Direct numerical simulation of turbulent pipe flow at moderately high Reynolds numbers. Flow, turbulence and combustion 91, 475–495.

He, S., He, K., Seddighi, M., 2016. Laminarisation of flow at low Reynolds number due to streamwise body force. Journal of Fluid Mechanics 809, 31–71.

He, S., Jiang, P.X., Xu, Y.J., Shi, R.F., Kim, W., Jackson, J., 2005. A computational study of convection heat transfer to CO2 at supercritical pressures in a vertical mini tube. International journal of thermal sciences 44, 521–530.

He, S., Kim, W., Bae, J., 2008. Assessment of performance of turbulence models in predicting supercritical pressure heat transfer in a vertical tube. International Journal of Heat and Mass Transfer 51, 4659–4675.

He, S., Seddighi, M., 2013. Turbulence in transient channel flow. Journal of Fluid Mechanics 715, 60–102.

Jackson, J., Cotton, M., Axcell, B., 1989. Studies of mixed convection in vertical tubes. International Journal of Heat and Fluid Flow 10, 2–15.

Jackson, J., Lutterodt, K., Weinberg, R., 2003. Experimental studies of buoyancy-influenced convective heat transfer in heated vertical tubes at pressures just above and just below the thermodynamic critical value, in: Proceedings of the Joint International Conference on Global Environment and Nuclear Energy System/Advanced Power Plants, pp. 15–19.

Jiang, P., Lu, Z., Guo, Y., Zhu, Y., 2019. Experimental investigation of convective heat transfer of hydrocarbon fuels at supercritical pressures within rotating centrifugal channel. Applied Thermal Engineering 147, 101–112.

Jiang, P.X., Wang, Z.C., Xu, R.N., 2018. A modified buoyancy effect correction method on turbulent convection heat transfer of supercritical pressure fluid based on RANS model. International Journal of Heat and Mass Transfer 127, 257–267.

Koshizuka, S., Takano, N., Oka, Y., 1995. Numerical analysis of deterioration phenomena in heat transfer to supercritical water. International Journal of Heat and Mass Transfer 38, 3077–3084.

Kurganov, V., Kaptil'Ny, A., 1992. Velocity and enthalpy fields and eddy diffusivities in a heated supercritical fluid flow. Experimental thermal and fluid science 5, 465–478.

Lee, S.H., Howell, J.R., 1998. Turbulent developing convective heat transfer in a tube for fluids near the critical point. International Journal of Heat and Mass Transfer 41, 1205–1218.

Lemmon, E., Huber, M., McLinden, M., 2010. Nist standard reference database 23, reference fluid thermodynamic and transport properties (refprop), version 9.0, national institute of standards and technology. R1234yf. fld file dated December 22, 2010.

Li, X., Hashimoto, K., Tanahashi, M., Miyauchi, T., 2007. Numerical study of heat transfer mechanism in turbulent supercritical CO2 channel flow, in: ASME/JSME 2007 Thermal Engineering Heat Transfer Summer Conference collocated with the ASME 2007 InterPACK Conference, American Society of Mechanical Engineers Digital Collection. pp. 247–256.

Licht, J., Anderson, M., Corradini, M., 2009. Heat transfer and fluid flow characteristics in supercritical pressure water. Journal of Heat Transfer 131, 072502.

Nemati, H., Patel, A., Boersma, B.J., Pecnik, R., 2015. Mean statistics of a heated turbulent pipe flow at supercritical pressure. International Journal of Heat and Mass Transfer 83, 741–752.

Nemati, H., Patel, A., Boersma, B.J., Pecnik, R., 2016. The effect of thermal boundary conditions on forced convection heat transfer to fluids at supercritical pressure. Journal of Fluid Mechanics 800, 531–556.

Peeters, J.W., Pecnik, R., Rohde, M., Van Der Hagen, T., Boersma, B.J., 2016. Turbulence attenuation in simultaneously heated and cooled annular flows at supercritical pressure. Journal of Fluid Mechanics 799, 505–540.

Pioro, I.L., Khartabil, H.F., Duffey, R.B., 2004. Heat transfer to supercritical fluids flowing in channels—empirical correlations (survey). Nuclear engineering and design 230, 69–91.

Popov, V., Belyaev, V., EP, V., 1977. Calculation of heat transfer and resistance by turbulent flow in a circular pipe of fluids with various types of temperature dependence of physical properties. Teplofiz. Vys. Temp 15, 1220–1229.

Pucciarelli, A., Borroni, I., Sharabi, M., Ambrosini, W., 2015. Results of 4-equation turbulence models in the prediction of heat transfer to supercritical pressure fluids. Nuclear Engineering and Design 281, 5–14.

Pucciarelli, A., Sharabi, M., Ambrosini, W., 2016. Prediction of heat transfer to supercritical fluids by the use of algebraic heat flux models. Nuclear Engineering and Design 297, 257–266.

Seddighi, M., 2011. Study of turbulence and wall shear stress in unsteady flow over smooth and rough wall surfaces. Ph.D. thesis. University of Aberdeen.

Shiralkar, B., Griffith, P., 1970. The effect if swirl, inlet conditions, flow direction, and tube diameter on the heat transfer to fluids at supercritical pressure. Journal of Heat Transfer 92, 490–497.

Tian, R., Wang, D., Zhang, Y., Ma, Y., Li, H., Shi, L., 2019. Experimental study of the heat transfer characteristics of supercritical pressure R134a in a horizontal tube. Experimental Thermal and Fluid Science 100, 49–61.

Tian, R., Zhang, Y., Ma, Y., Li, H., Shi, L., 2018. Experimental study of buoyancy effect and its criteria for heat transfer of supercritical R134a in horizontal tubes. International Journal of Heat and Mass Transfer 127, 555–567.

Valori, V., Elsinga, G.E., Rohde, M., Westerweel, J., van Der Hagen, T.H., 2019. Particle image velocimetry measurements of a thermally convective supercritical fluid. Experiments in Fluids 60, 143.

Vukoslavčević, P.V., Radulović, I.M., Wallace, J.M., 2005. Testing of a hot- and cold-wire probe to measure simultaneously the speed and temperature in supercritical CO2 flow. Experiments in fluids 39, 703–711.

Wang, W., He, S., 2015. Mechanisms of buoyancy effect on heat transfer in a horizontal flow, in: Proceedings of the 7th International Symposium on Supercritical Water-Cooled Reactors (ISSCWR-7), pp. 15–18.

Xu, K., Ruan, B., Meng, H., 2018. Validation and analyses of RANS CFD models for turbulent heat transfer of hydrocarbon fuels at supercritical pressures. International Journal of Thermal Sciences 124, 212–226.

Yamagata, K., Nishikawa, K., Hasegawa, S., Fujii, T., Yoshida, S., 1972. Forced convective heat transfer to supercritical water flowing in tubes. International Journal of Heat and Mass Transfer 15, 2575–2593.

Yan, J., Zhu, Y., Zhao, R., Yan, S., Jiang, P., 2018. Experimental investigation of the flow and heat transfer instabilities in n-decane at supercritical pressures in a vertical tube. International Journal of Heat and Mass Transfer 120, 987–996.